

Variational Autoencoders for Jet Simulation

Kosei Dohi

21kdohi@tenafly.k12.nj.us

Tenafly High School

Tenafly, NJ 07670 USA

Abstract

We introduce a novel variational autoencoder (VAE) architecture that can generate realistic and diverse high energy physics events. The model we propose utilizes several techniques from VAE literature in order to simulate high fidelity jet images. In addition to demonstrating the model's ability to produce high fidelity jet images through various assessments, we also demonstrate its ability to control the events it generates from the latent space. This can be potentially useful for other tasks such as jet tagging, where we can test how well jet taggers can classify signal from background for events generated by the VAE. We test this idea by seeing the signal efficiency vs background rejection for different types of jet images produced by our model. We compare our VAE with generative adversarial networks (GAN) in several ways, most notably in speed. The architecture we propose is ultimately a fast, stable, and easy-to-train deep generative model that demonstrates the potential of VAEs in simulating high energy physics events.

Contents

1	Introduction	1
2	Methods	2
2.1	Variational Autoencoder	2
2.2	Data	4
2.3	Model Architecture	5
3	Model Assessment	8
4	Exploring the Latent Space	14
5	Speed Comparison	22
6	Conclusion	23

1 Introduction

Deep generative models used in high energy physics simulation have shown promising performances due to their ability to produce data in record times [1–27]. Many of the calorimeter-based events that produce 2D images, such as jets and electromagnetic showers, utilize generative adversarial networks (GAN) to generate these events [28–30]. Although GANs have demonstrated to excel in simulating diverse and accurate radiation patterns, there are various other models that can be explored that can achieve similar results and alleviate previous problems with GANs. One problem with GANs, for example, is that they can be difficult to train and produce classes of images that are too distinguishable from each other [1]. An alternative model that can solve these potential problems is the variational autoencoder (VAE) [31]. The VAE is an extension of the autoencoder (AE) and consists of the same principal components of the autoencoder – the encoder, the latent space, and the decoder. In addition to these components, the VAE adds a sampling layer that allows the model to generate new data from the latent space. More detail can be found in section 2.1.

The application of GANs in various domains have highlighted its strong ability to produce crisp images [32, 33]. This has ultimately made the GAN a popular choice for image generation. On the other hand, VAEs are known to produce noisier images due to the nature of its latent space and how images are generated from it. However, with recent progress in

VAE research, VAEs have become comparable to GANs in producing highly realistic images for a wide variety of fields [34–40]. A good example of VAEs specifically used in high energy physics is for generating electromagnetic and parton showers [41, 42]. Models such as the Introspective VAE [43] and the Vector-Quantised VAE [44] have also shown to produce high resolution face images that are comparable to the state-of-the art GANs. Autoencoders and unsupervised/weakly supervised machine learning models, in general, have been applied to a wide variety of fields including in high energy physics [45–67].

One of the key characteristics of the VAE that allows it to be a diverse generative model is its latent space. With its latent space, the VAE can control what kind of features it generates. A simple example with face images would be adding facial features, such as a smile, to the images being generated by the VAE. Following a similar idea, calorimeter deposits can be fed through a VAE to produce images with certain types of features such as the outer radiation of a jet.

In this paper, we propose a novel VAE architecture that can be used to simulate jet images. The model uses a variety of techniques from VAE/GAN research to help generate the sparse features of jet images. We test the model through certain qualitative and quantitative assessments and also observe the latent space to see what kind of features the VAE learns and how it can be used to simulate jets with diverse properties.

2 Methods

The methods section is organized as follows. We start by describing how vanilla autoencoders and variational autoencoders work. Afterward, we briefly describe the dataset we used to train the model. And finally, we talk about the architecture of the model we propose and its training process.

2.1 Variational Autoencoder

To provide a better understanding of the variational autoencoder, we first provide a brief overview of the autoencoder. The autoencoder consists of three main components: the encoder, the decoder, and the latent space. The encoder takes input data, in our case, a dataset of images, and compresses it into the latent space using neural networks. The latent space is where all the information is stored and the goal is to optimize how data is scattered in this latent space. The decoder, on the other hand, is a mirror of the encoder because it tries to recreate the input data from the compressed latent space.

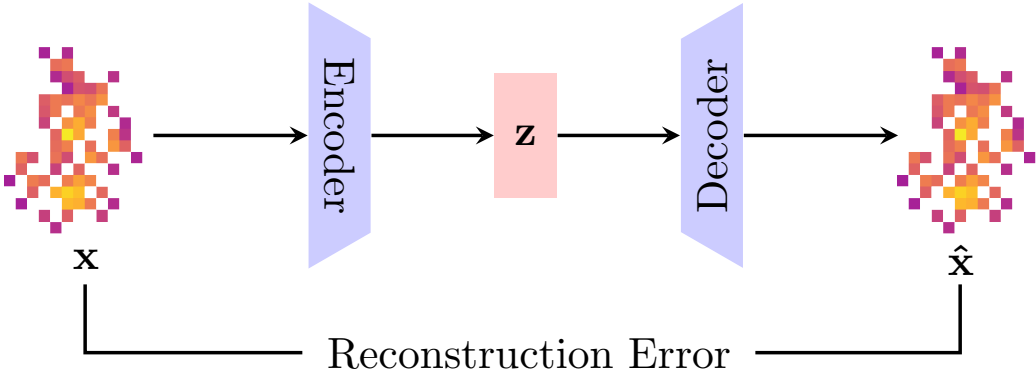


Figure 1: Simple schematic of the autoencoder. The input image, denoted by X , is fed through the encoder and into a latent dimension z . The decoder then tries to reconstruct the input image from the latent space to get a predicted output image denoted by \hat{X} .

The goal of the autoencoder is to ultimately provide a dimensionality reduction algorithm that learns to encode data by optimizing a distance metric loss. The better the encoder learns to compress data, the better the reconstructed image will be. A common loss function used for the autoencoder is the mean squared error, which takes the squared difference between the input and output image.

$$\frac{1}{n} \sum_{i=1}^n (\hat{X} - X)^2 \quad (2.1)$$

A variational autoencoder is a generative model that follows a similar structure to the vanilla autoencoder. The reason why a normal autoencoder isn't able to generate new data is because it encodes input data into discrete values in the latent space. This process only allows the autoencoder to “memorize” the input data. To contrast this, the variational autoencoder encodes the input data into a sampling layer that makes the latent space continuous. This process allows the decoder of the variational autoencoder to generate new and realistic data using the learned features from the latent space. The latent space of the variational autoencoder can be explored because images with certain features in the latent space will be closer together than ones in another region.

The objective of the VAE can be mathematically described with the following equation:

$$\mathcal{L}(\theta, \phi; X) = \underbrace{E[\log P_\theta(X|z)]}_{\text{Reconstruction term}} - \underbrace{D_{KL}[Q_\phi(z|X)||P_\theta(z)]}_{\text{KL Divergence}} \quad (2.2)$$

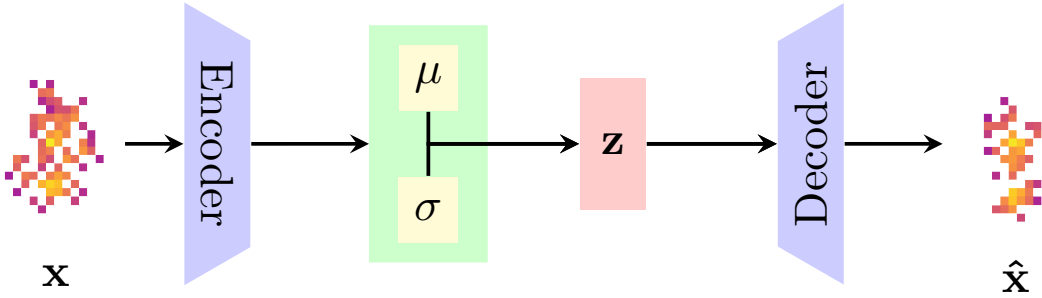


Figure 2: Simple schematic of the variational autoencoder. The input image is fed through the encoder and into a sampling layer, represented by the green box. The sampling layer maps the image into a Gaussian distribution with a certain mean (μ) and standard deviation (σ). This allows the decoder to sample from a continuous latent space, or, in other words, enables it to generate images using features from input X .

Where the encoder system is denoted by $Q_\phi(z|X)$, the latent space is denoted by z , and the decoder system is denoted by $P_\theta(X|z)$. The Kullback-Divergence loss (D_{KL}), which is a loss function that helps ensure that the output of the encoder doesn't deviate from the posterior distribution $P(z)$, can be described with the following equation

$$D_{KL} = \frac{1}{2} \sum_k (\exp(\sigma) + \mu^2 - 1 - \log(\sigma)) \quad (2.3)$$

Where μ and σ represents the mean and standard deviation of the Gaussian distribution used to generate data. The $E[\log P(X|z)]$ term in the variational autoencoder objective is a reconstruction term that measures how well generated data from $P(X|z)$ (decoder) can represent the input data X .

2.2 Data

The dataset we use in this research is the one used in the Location-Aware Generative Adversarial Network paper [1]. We directly download from the Zenodo website their preprocessed jet images which consist of W boson and QCD jet images [68]. We will give a brief summary of the dataset, however, more detail is found in the source paper. The jet images are simulated with Pythia 8.219 [69, 70] at 14 TeV and are clustered with FastJet [71]. The p_T range is set between $250 \text{ GeV} < p_T < 300 \text{ GeV}$ and the jets are trimmed and translated so that the subjet with the highest p_T is set at the origin of the image and the second subjet is

placed at $-\pi/2$ relative to the $\eta - \phi$ space. The image is graphed with the grid coordinates:

$$\eta \times \phi \in [-1.25, 1.25] \times [-1.25, 1.25] \quad (2.4)$$

This ultimately leads to the production of 25×25 images where the pixel intensities represent the total p_T . The total p_T corresponds to the equation:

$$p_T = E_{cell}/\cosh(\eta_{cell}) \quad (2.5)$$

Where E_{cell} and η_{cell} is the energy and pseudorapidity of the calorimeter cells respectively. Once again, a more in-depth detail of the simulation process is found in the paper where we got our dataset.

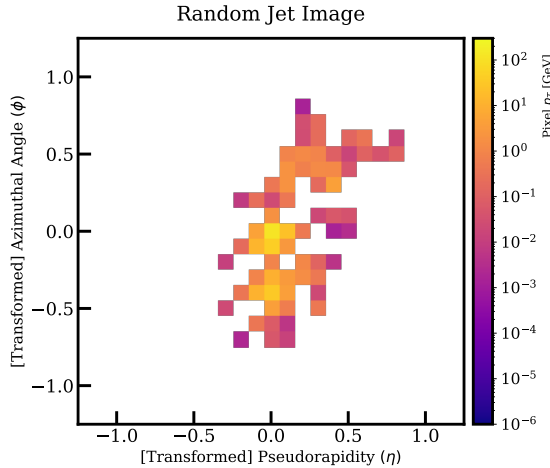


Figure 3: A random jet image.

2.3 Model Architecture

The model we propose is a vanilla VAE that uses a variety of techniques in VAE literature. The first technique we use borrows from the idea of a Conditional Variational Autoencoder (CVAE) [72]. Since a normal VAE randomly scatters data in the latent space, it is unable to produce images from a certain class. To alleviate this, a CVAE conditions a categorical label to both the input data and the latent space. Because the model we propose uses convolutional layers and it is difficult to combine a three dimensional $25 \times 25 \times 1$ image to a one dimensional class label, we use a RepeatVector layer that creates a $25 \times 25 \times 2$ image of the categorical class label. This ultimately results in a $25 \times 25 \times 3$ input when combined with the input image. This process was important in producing W boson and QCD jet images

with distinct features.

With the $25 \times 25 \times 3$ image, we pass through an encoder that consists of three convolutional layers with filters of 32, 64, 128 respectively. A kernel size of 3 is used for all layers, the padding is same for all layers, and strides of 2 are used only for the second and third convolutional layers of the encoder. We flatten the last convolutional layer of the encoder and pass the flattened image into the latent space. The categorical label is conditioned to the latent space, which is then passed through a dense layer of 6272 and reshaped to a dimension of $7 \times 7 \times 128$. This then goes through a decoder that consists of two deconvolutional layers with filters of 64, 32 respectively, kernel sizes of 3, and strides of 2. For the last convolutional layer, we put a convolutional layer with 1 filter, valid padding, and a kernel size of 4 to return to a $25 \times 25 \times 1$ image. All convolutional layers use LeakyReLU activation functions except for the last layer, which uses relu as recommended in [1].

To further amplify the quality of the jet images, we take the sum of the KL divergence, feature perceptual and Bernoulli loss as our loss function. Normally, a VAE uses the KL divergence loss paired with some simple distance metric such as the mean squared error. We use the feature perceptual loss as our distance metric loss instead due to the higher quality images it produces [73, 74].

The feature perceptual loss takes the squared difference between the hidden features of the input and output image of the VAE. The hidden features are calculated by a pretrained convolutional neural network that is excluded from the optimization process of the model. The loss function is mathematically described as:

$$\begin{aligned} \mathcal{L}_{perceptual}^i &= \frac{1}{2C^i W^i H^i} \sum_{c=1}^{C^i} \sum_{w=1}^{W^i} \sum_{h=1}^{H^i} (\Phi(\hat{X})^i - \Phi(X)^i)^2 \\ \mathcal{L}_{perceptual} &= \sum_i (w_i \times \mathcal{L}_{perceptual}^i) \end{aligned} \quad (2.6)$$

Where $\Phi(X)$ and $\Phi(\hat{X})$ are the predicted features, taken from the i th layer in the convolutional neural network, of the input and output images and C, W, H is the channel, width, and height of the images respectively. The total loss is calculated by combining the feature perceptual loss for i layers in the convolutional neural network with a weight, denoted by w_i , for each loss. The weight can be adjusted to put emphasis on certain layers when calculating the loss. For simplicity, we set the weight for each perceptual loss as 1.

We found that the feature perceptual loss was a crucial component in capturing the sparse radiation patterns and the prongs of the jet images. Because of this, the use of locally-connected layers, which was recommended in [1], was not needed. In addition to the

feature perceptual loss, we add a Bernoulli loss function. Because the Bernoulli loss requires gray scale images, we normalize the images by dividing them by 100. We also transform both the input and output image to 625 dense layers when calculating this loss. We found that using this loss helped produce slightly better sparsity.

This makes the total loss function of the VAE:

$$\mathcal{L}_{VAE} = \mathcal{L}_{perceptual} + \mathcal{L}_{KL} + \mathcal{L}_{Bernoulli} \quad (2.7)$$

The convolutional neural network for calculating the feature perceptual loss uses three convolutional layers with three dense layers. We tested how various kernel sizes and filters affected the performance of the VAE to see which classifier architecture was optimal. We found that using relatively large kernel sizes paired with 32 filters in the first convolutional layer was able to teach the VAE how to produce the central region of the jets. We ultimately settled on using a kernel size of 11 with 32 filters. The second layer, as our investigations showed, helped in producing the sparse radiation patterns of the jet images. We found that using small kernel sizes of 3 or 5 and 64 filters was able to produce sparse jet images. We ultimately decided to settle on a kernel size of 5. We found that the third layer, which had 64 filters and a kernel size of 5, was not necessary in calculating the feature perceptual loss and even worsened performance.

Each convolutional layer uses strides of two and are followed by a Dropout layer. The LeakyReLU activation is also used for each convolutional layer. The convolutional layers in the classifier are followed by three dense layers of 128, 64, and 1, where the last layer has a sigmoid activation function. The model is trained for 50 epochs with a batch size of 100 and uses the Adam optimizer. The loss for the classifier is the binary crossentropy loss.

$$BCE = (y)(-\log(y_{pred}) + (1 - y)(-\log(1 - y_{pred})) \quad (2.8)$$

To clarify, we use the same dataset to train the classifier as the one used to train the VAE. This means the classifier is doing a binary classification on W boson and QCD jet images.

We trained multiple VAE models and found that the latent size was also crucial in producing sparse jet images. We found that a large latent size of 10-15 produced jet images with good sparsity and prominent jet prongs. Anything below 6 didn't produce as much sparsity but the jet prongs were preserved. Anything higher than 15 produced jet images with unrealistic sparsity levels. This ultimately makes sense because the latent size is where information is stored, therefore, a bigger latent size will store more information while a

smaller one will limit information. In this case, more information is equivalent to capturing more sparsity in the jet images. We found that a latent size of 12 was a good dimension for $25 \times 25 \times 1$ images. The latent size should ultimately vary depending on the dimension of the input data and the type of data being used.

We build all models, including the feature perceptual classifier, in Keras [75] with a Tensorflow backend [76]. We use the Adam optimizer and train the VAE for 12 epochs with a batch size of 100. The model is trained in Kaggle which uses a NVidia K80 GPU.

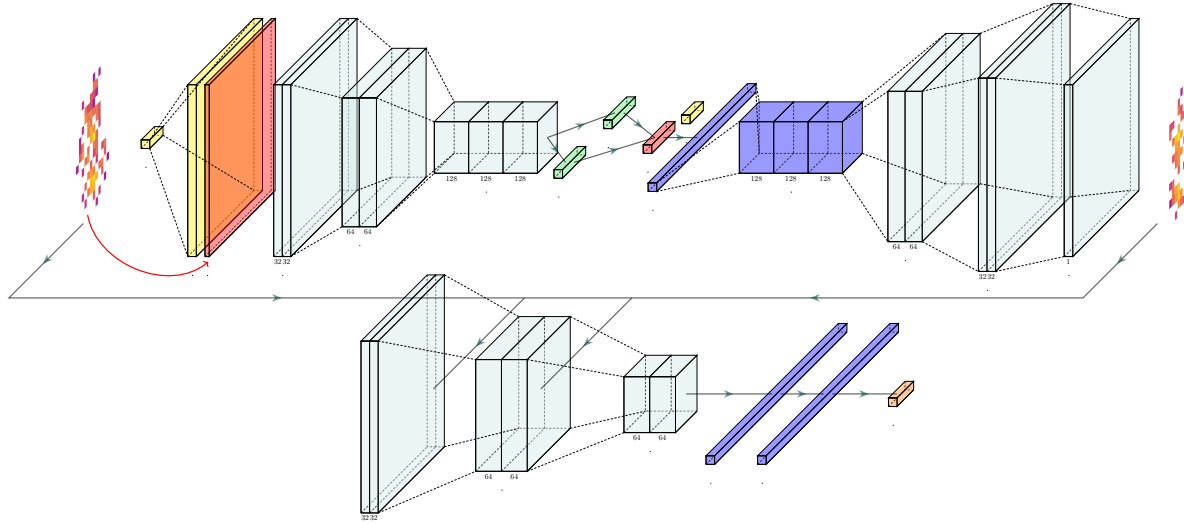


Figure 4: The architecture of our VAE model. The VAE starts off by passing the categorical label through a RepeatVector layer. This 3D categorical image label is then combined with the input image, resulting in a $25 \times 25 \times 3$ input. This input is passed through the encoder, which then goes through a sampling layer. The latent space is concatenated to the label, passed through a dense 6272 layer, reshaped to $7 \times 7 \times 128$, then passed through the decoder. The input and output images are compared with the hidden features of the first two layers in the classifier.

3 Model Assessment

For our assessment, we compare 300,000 VAE and Pythia jet images. We begin our VAE assessment by graphing a histogram of the pixel intensities of both Pythia and VAE jet images in Figure 5. The pixel distribution helps assess whether or not the VAE can successfully learn a wide variety of pixel intensities. In this case, the VAE is shown to explore high and low levels of pixel intensities and is able to match the overall pixel distribution of the Pythia

jet images. Similarly, we can measure the difference between Pythia and VAE by taking the mean squared error of their jet images. We also calculate the MSE between Pythia and the Location-Aware Generative Adversarial Network (LAGAN) [77] jet images. Both values are shown in Table 1. The VAE is shown to have a slightly smaller difference with Pythia jet images in comparison to the LAGAN.

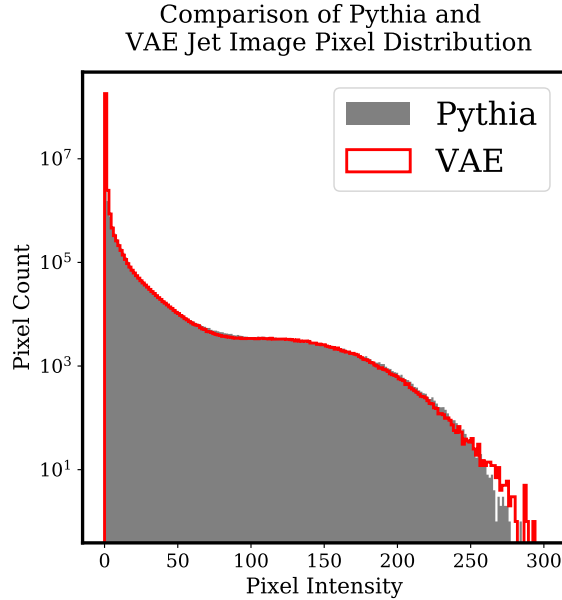


Figure 5: Pixel distribution of Pythia and VAE jet images.

Table 1: Mean Squared Error (MSE) of Pythia jets with VAE and LAGAN jets.

Model	MSE
VAE	17.27
LAGAN	19.29

Another useful way to assess our VAE model is to see whether or not its jet images can recreate some of the jet observables of the Pythia jet images. In this study, we calculate the mass, p_T , and N-subjettiness [78] of both Pythia and VAE jet images and compare them in Figure 6. The VAE is shown to match the general shape of the Pythia jet observables, however, it struggles in certain areas. This is especially noticeable in the mass of the QCD jet images. This is further highlighted in Table 2, where the mean and standard deviation of the VAE distributions are shown. The VAE does a slightly poorer job in matching the Pythia distribution than the LAGAN. Despite the effectiveness of the feature perceptual loss, the VAE still produces blurrier images, especially for sparse features. This can be seen

in Figure 7 where the jet images are shown to be “smudged”. Additional modifications, such as adding additional loss functions and constraints, may be able to mitigate this problem.

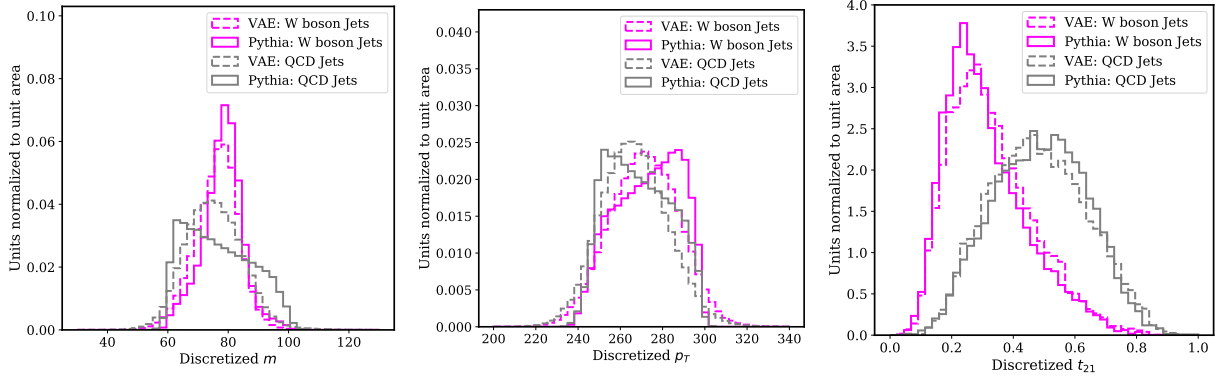


Figure 6: Mass, p_T , and N-subjettiness distributions for Pythia and VAE jet images.

Model	Mass		p_T		t_{21}	
	μ	σ	μ	σ	μ	σ
Pythia (W boson)	78.19	6.77	273.12	14.91	0.31	0.13
VAE (W boson)	76.16	7.34	271.08	14.51	0.33	0.14
LAGAN (W boson)	79.64	7.24	276.27	14.81	0.28	0.09
Pythia (QCD)	76.91	11.01	268.64	14.82	0.49	0.15
VAE (QCD)	75.29	9.40	266.03	14.08	0.48	0.16
LAGAN (QCD)	77.62	13.30	267.06	19.44	0.51	0.13

Table 2: Mean and standard deviation of jet observable distributions.

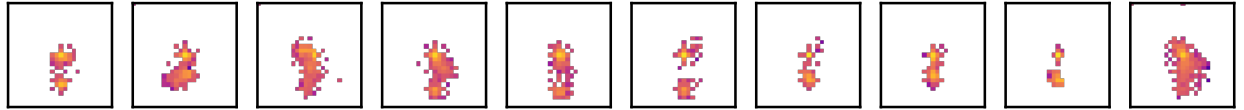


Figure 7: 10 random VAE jet images. The images highlight that the VAE, despite using the feature perceptual loss, can still produce slightly blurry images.

To provide a more visual assessment of what kind of jet images the VAE produces, we take the average jet image for both Pythia and VAE jet images in Figure 8. The average VAE jet image is shown to reproduce the jet constituents well along with some of the outer radiation. One problem outlined by the average VAE jet image is that some of the radiation towards the bottom left is missing. This may happen due to the nature of the feature

perceptual loss. When the classifier is calculating the loss between the input and output image, parts of the hidden features may be empty due to the use of same padding in the first and second layers of the classifier. To avoid this, it may be best to avoid same padding in the classifier altogether. Despite this problem, we support the claim that the VAE is able to reproduce the central region of the Pythia jet images by taking the difference between the average Pythia and average VAE jet image in Figure 9. We also include the difference between the average Pythia jet image with the average jet image from the LAGAN.

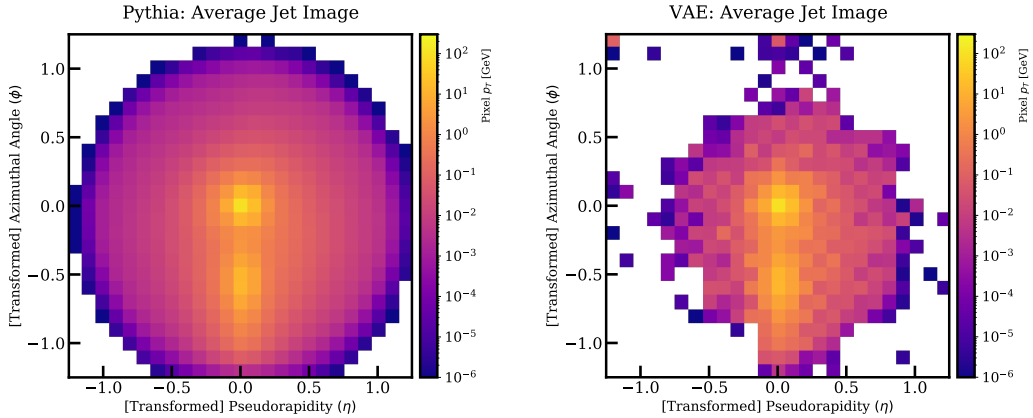


Figure 8: Average jet image for Pythia and VAE jet images.

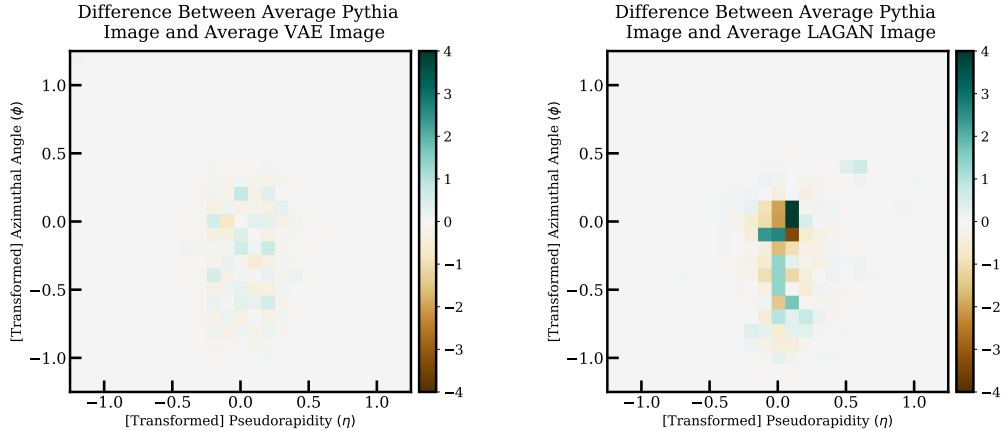


Figure 9: Difference between the average Pythia jet image with the average VAE and LAGAN jet image.

The central component of the VAE jet image is shown to be similar to the central component of the Pythia jet image due to the little variation there is between the two images. This is strongly correlated to the feature perceptual loss and the latent size we used. Without the use of the feature perceptual loss, we found that the VAE did a significantly poorer job

in producing the central component of its jet images. Using big kernel sizes and a relatively small number of filters for the first layer of the classifier used for the feature perceptual loss also helped reinforce the learning of the central region. In addition to the feature perceptual loss, the latent size we chose was also crucial for producing the central component of the jets. Having too big of a latent size negatively affected the intensities towards the center. We did see, however, that the central region was well produced even with latent space sizes smaller than 10. This is most likely the case because the central region of the jet images is a more prominent feature, therefore, the VAE will learn this feature much more consistently. To compare our VAE with previous generative models, we also include the difference between the average Pythia jet image and the average LAGAN jet image. The LAGAN is shown to struggle more in producing the central component of its jets due to the strong positive and negative correlations shown in the image. To quantitatively measure Figure 9, we calculate the Structural Similarity Index (SSIM) of the average Pythia image with the average VAE and LAGAN image in Table 3. The table ultimately demonstrates that the VAE can reproduce the central region of the jet images significantly better than the LAGAN.

Table 3: Structural Similarity Index (SSIM) of the average Pythia jet image with the average VAE and LAGAN jet image. The closer the SSIM is to 1, the better the performance.

Model	SSIM
VAE	0.94
LAGAN	0.85

To evaluate the VAE’s ability to generate different classes of images, we take the difference between the average W boson and QCD jet image produced by the VAE. This is an important evaluation because the features between the two classes of images should be noticeable. In this case, we want to see the outer radiation of the QCD jet images and the jet prongs from the W boson jet images. This was one of the shortcomings of the LAGAN because the model overestimated the importance of certain features in its jet images. To compare the distinguishability of W boson and QCD jet images, we take the difference between the average W boson and average QCD jet images for Pythia, VAE, and LAGAN in Figure 10.

The VAE is shown to have almost identical differences in its W boson and QCD jet image with the W boson and QCD jet images of Pythia. The radiation pattern of the QCD jet image and the jet prongs of the W boson jet image is visible in the VAE. This contrasts the LAGAN, where the radiation of the QCD jet image is more prominent than it should be.

We further explore the similarity of W boson and QCD jet images by taking the predicted

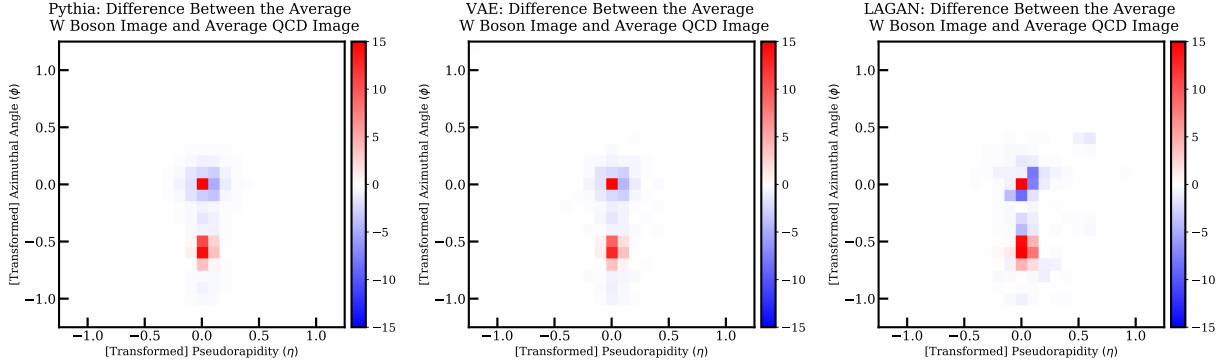


Figure 10: Difference between the average W boson and QCD jet image for Pythia, VAE, and LAGAN.

class probabilities, calculated by the feature perceptual loss classifier, of the jet images in Figure 11. This classifier was trained with Pythia jets only, so the ultimate goal is to match the Pythia curve. 0 represents a prediction of background and 1 represents a prediction of signal. The classifier predicts Pythia, VAE, and LAGAN jets.

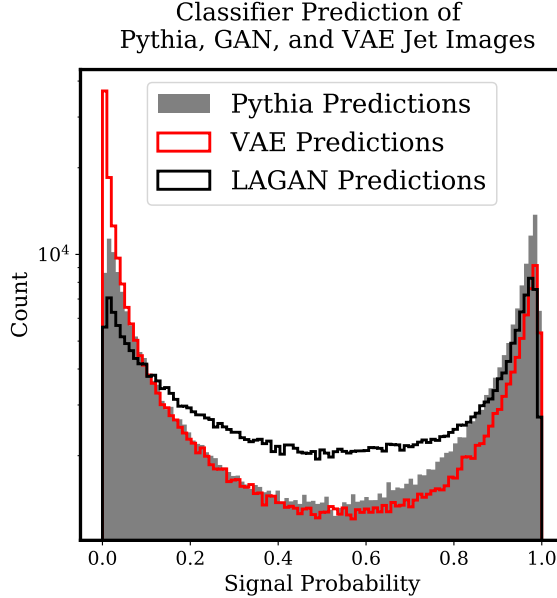


Figure 11: Classifier class probability predictions for Pythia, VAE, and LAGAN jet images. 0 represents a background prediction and 1 represents a signal prediction. The VAE is shown to produce QCD jet images that are easier to classify. The overall distribution, however, is shown to match a good majority of the Pythia distribution.

We can see that the distribution of the Pythia jet images has a nice symmetrical distribution. The VAE is shown to have slightly higher predictions for background and slightly lower predictions for signal. Although the VAE curve is not perfect, it is ultimately

able to match a good majority of the Pythia predictions. The LAGAN predictions are symmetrical, however, there is more uncertainty when classifying its jet images. This is demonstrated with the higher counts towards the center of the distribution.

4 Exploring the Latent Space

A key feature of the variational autoencoder is its latent space. This is where all the information of the VAE is stored, therefore, it is important to see how the latent space affects what kind of jet images are produced. We start this section by displaying what are known as linear interpolations. A linear interpolation is a series of images generated by a VAE that travels linearly through the Gaussian distribution used to simulate data. In this case, the distribution has a mean of 0 and a standard deviation of 1. The linear interpolation ultimately helps visualize what kind of features the VAE learns. We begin by showing a linear interpolation of QCD and W boson jets in Figures 12 and 14 and the difference between the two classes of images in Figure 13. Each column represents a different latent space value (1-12) in descending order.

The VAE is shown to have learned a diverse range of features in the latent space. Two examples include the slants found in the 10th latent space value and the growing radiation patterns in the 7th latent space value. These linear interpolations help us not only visualize more specific features that the VAE is learning, but it also demonstrates what kind of images are produced for each latent space value. A more detailed study is found later in this section.

We provide a more detailed analysis on how the features of the jets change by seeing how the mass, p_T , and N-subjettiness curves in Figures 15, 16, and 17 change in different regions of the $N(0, 1)$ distribution (the Gaussian distribution the decoder samples from). 50,000 jet image are used to generate each curve. These curves reveal several interesting characteristics of the VAE. The mass, p_T , and N-subjettiness of the W boson and QCD jet images shift in various directions throughout the $N(0, 1)$ distribution. A key pattern that we can see is that the spikes in the jet observable graphs start to flatten as the latent space value approaches 1. We visually inspect these patterns in Figure 18, which displays the average jet image for W boson and QCD jet images for each interval of the $N(0, 1)$ distribution and the difference between the two images in the middle column. A pattern that can be observed is that the outer radiation of the QCD jet image and the prongs of the W boson jet images start to become more prominent as they approach 1.

Due to the wide variety of curves that is produced by the VAE, the VAE can be potentially useful for certain tasks such as jet tagging. Specific jet images produced by VAE can be used

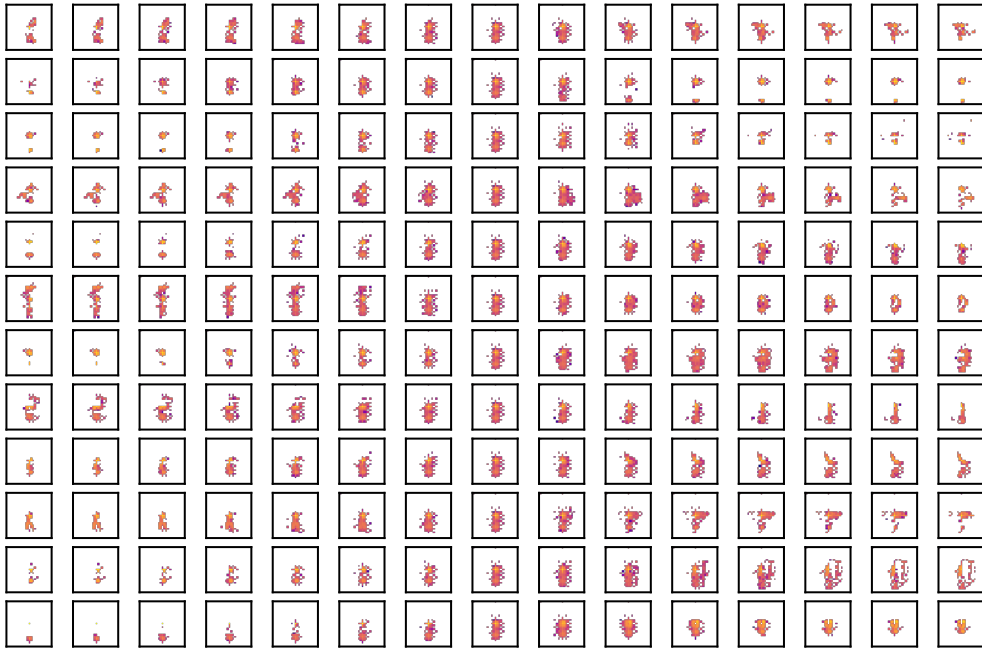


Figure 12: Linear Interpolation of QCD jet images.

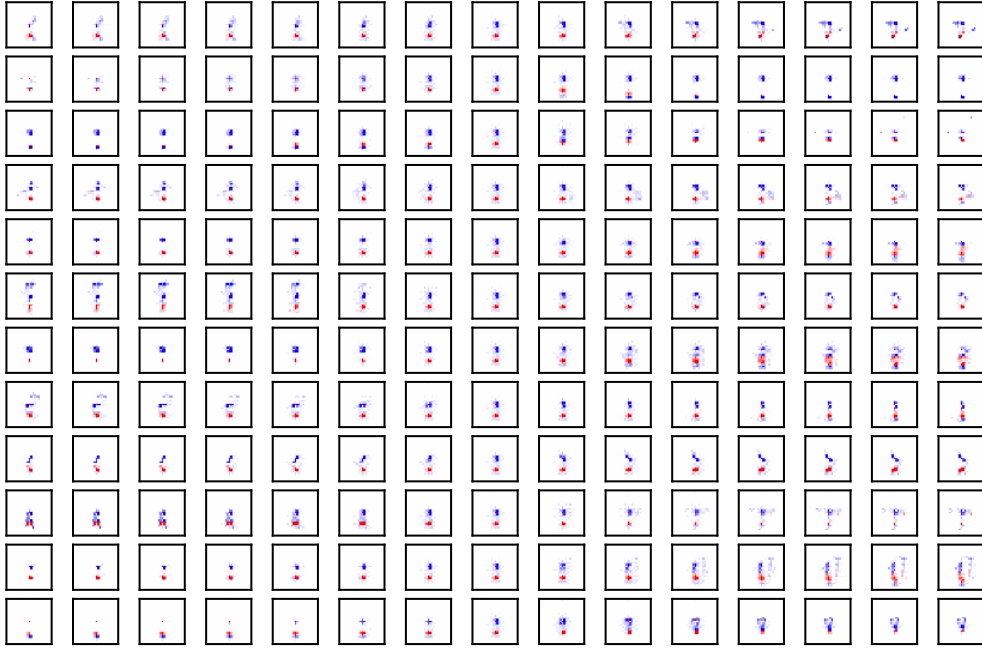


Figure 13: Difference in Linear Interpolation between W boson and QCD jet images.

to test certain taggers in distinguishing signal from background generated by various regions in $N(0, 1)$. For example, we can test how well a tagger can tag jet images in the $[0.75, 1]$ interval where the mass, p_T , and N-subjettiness distributions are very close together. By

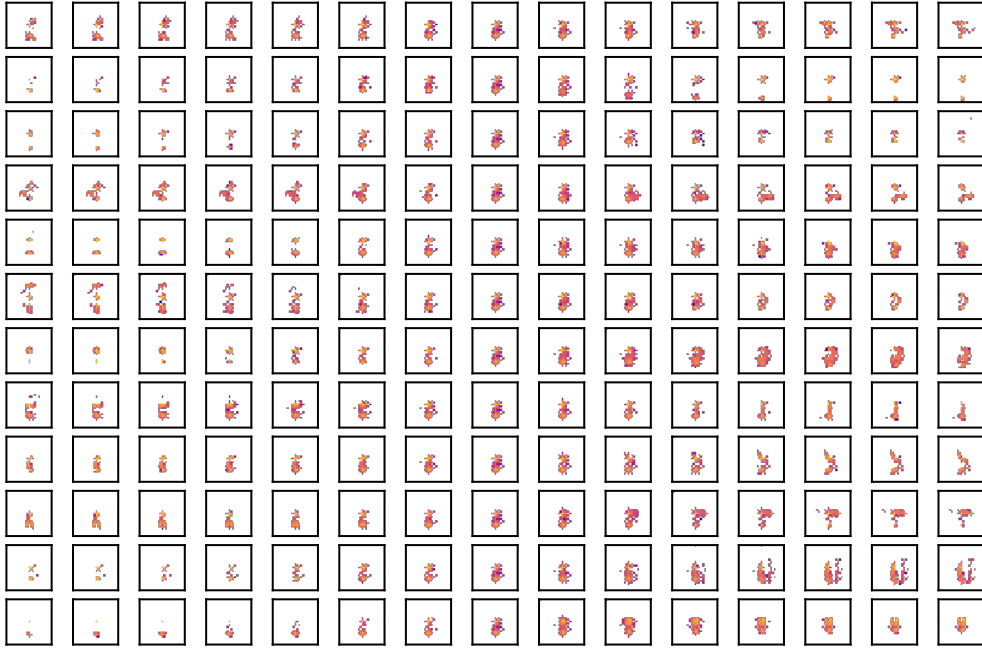


Figure 14: Linear Interpolation of W jet images.

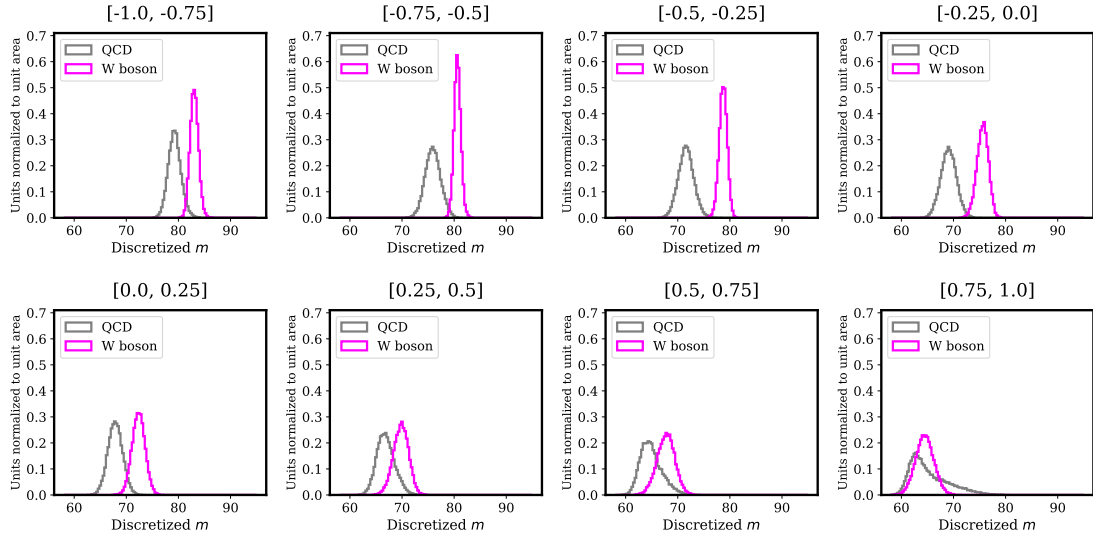


Figure 15: Mass distributions for various intervals in the $N(0, 1)$ distribution.

increasing the number of intervals in $N(0, 1)$, a wider variety of curves can be seen. For this assessment, we only use 8 intervals from this Gaussian distribution but a higher number can be used.

To support our claim, we plot the ROC curve of signal efficiency vs background rejection for various regions in $N(0,1)$. We test this on the mass and p_T of the jet images in Figures 19 and 20. The ROC curves demonstrate how the cut between signal and background can

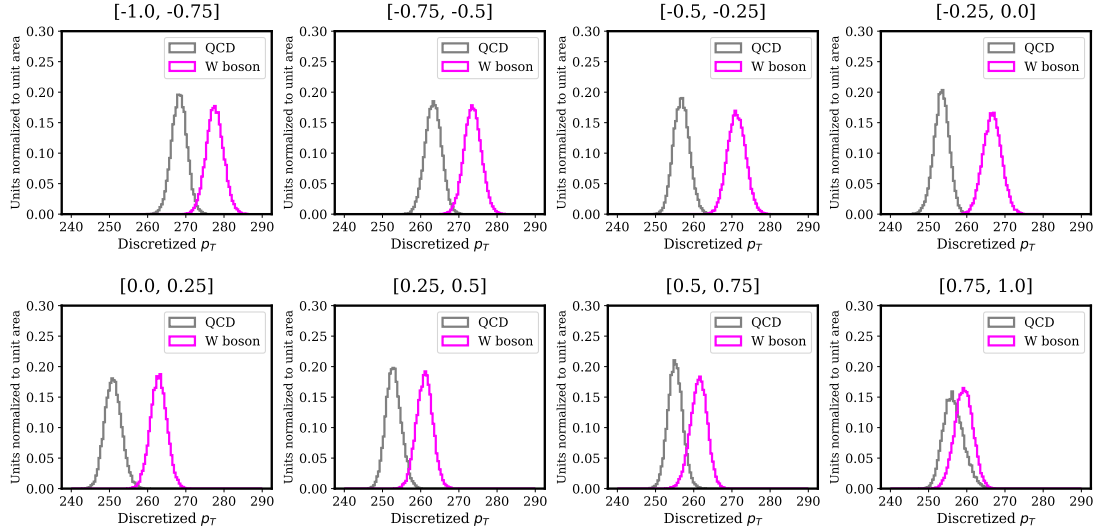


Figure 16: p_T distributions for various intervals in the $N(0, 1)$ distribution.

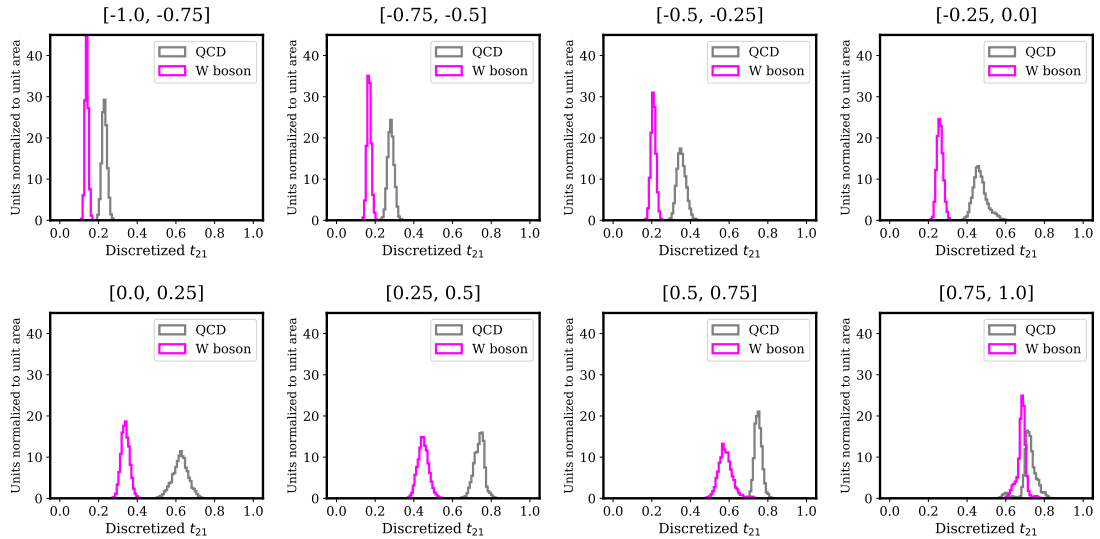


Figure 17: N-subjettiness distributions for various intervals in the $N(0, 1)$ distribution.

change for different kinds of jet images produced by the VAE. As shown in Figures 16 and 17, the distributions are harder to cut as we approach 1 in the $N(0,1)$ distribution. This is shown by the low Area Under the Curve (AUC) in Figures 19 and 20 from $[0.75, 1]$. We can further see how the distinctness of QCD and W boson jet images change in Figure 21. Because similar masses between jet images can be obtained from either two hard prongs or with one hard prong with a diffused spray, a more visual assessment can be observed by seeing how a classifier predicts W boson and QCD for various regions in $N(0,1)$. This supports Figure 18, where although the jet images have similar mass and p_T in the $[0.75, 1]$

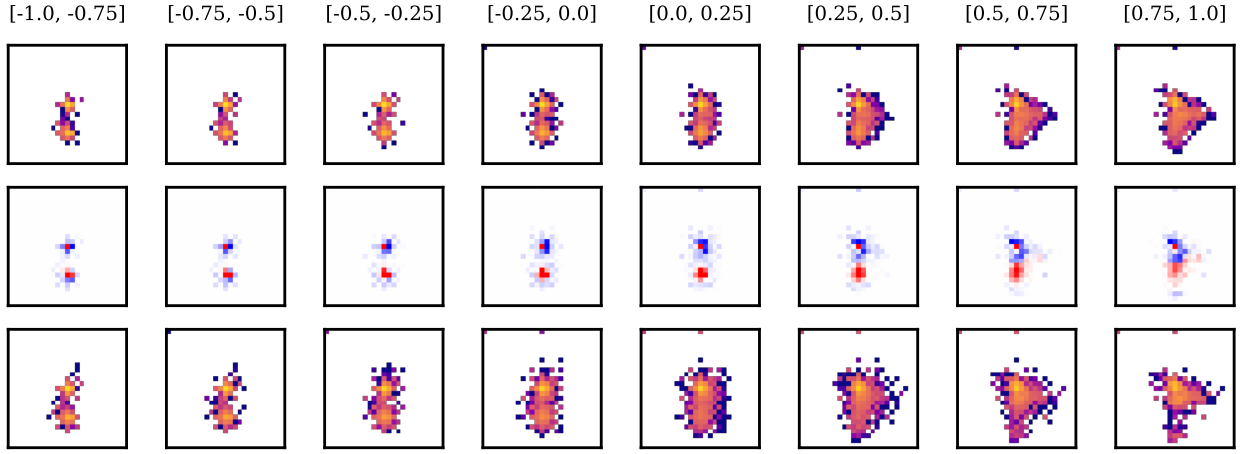


Figure 18: Average jet image for different intervals in the $N(0,1)$ distribution. The top column represents the average W boson jet image, the bottom represents the average QCD jet image, and the center column is the difference between the two images. We can see that the outer radiation of the QCD (blue) and the prongs of the W boson (red) jet image become more prominent as they approach 1.

region, they have visually different features.

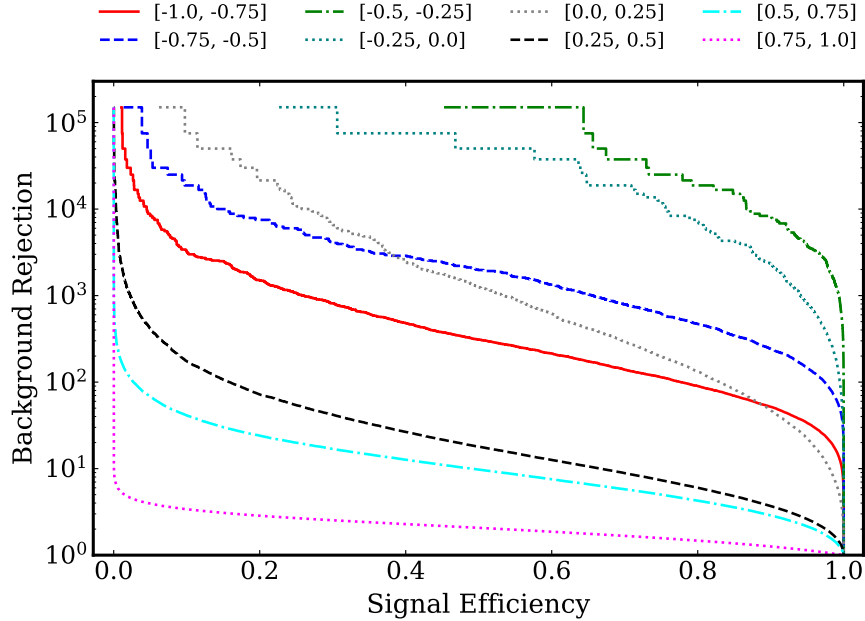


Figure 19: ROC curves (signal efficiency vs background rejection) for jet images, with a cut on mass, produced by different regions in $N(0,1)$. This illustrates how the cut between W boson and QCD jet images can be controlled by the VAE.

We further investigate the latent space by observing how each latent space value affects the overall distribution of data being produced. To analyze this, we set all other values in

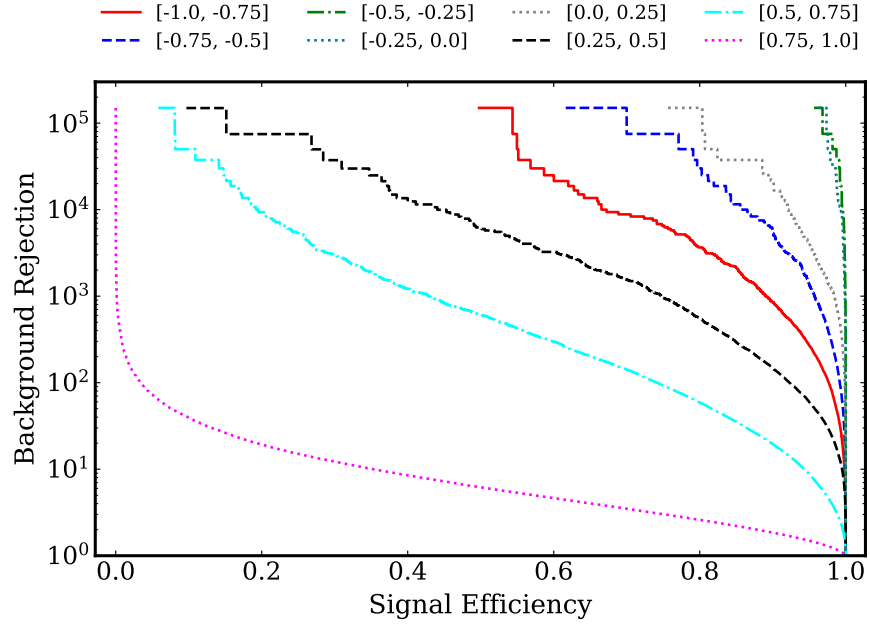


Figure 20: ROC curves (signal efficiency vs background rejection) for jet images, with a cut on p_T , produced by different regions in $N(0, 1)$.

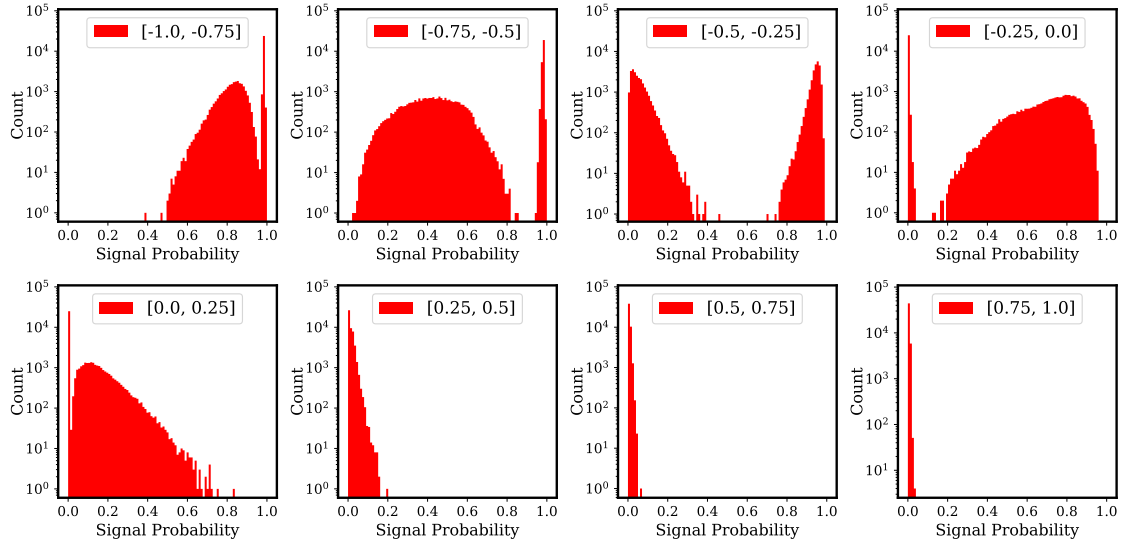


Figure 21: Classifier predictions of signal and background (0 represents background and 1 represents signal) for various regions in $N(0,1)$.

the latent size to zero except for the one we are analyzing and calculate the mass and p_T for the generated images. These graphs are shown in Figures 22 and 23. A diverse range of distributions is shown for different latent space values. These graphs are not necessarily realistic distributions of data because a VAE will normally utilize all latent space values,

but these figures highlight what kind of information is scattered throughout a latent space of 12. There are some subtle patterns found in the mass and p_T curves but not necessarily strong ones. For example, we can see a large spike in mass for the jet images produced from latent space values of 7 through 9 and a smoothing of the distributions generated by latent space values of 2 and 3. All latent space values are ultimately used by the VAE to create an aggregate of all these features. This is why the W boson jet images have large spikes in mass towards the center of the curves because it helps create the spike in mass found in the W boson mass distribution in Figure 6.

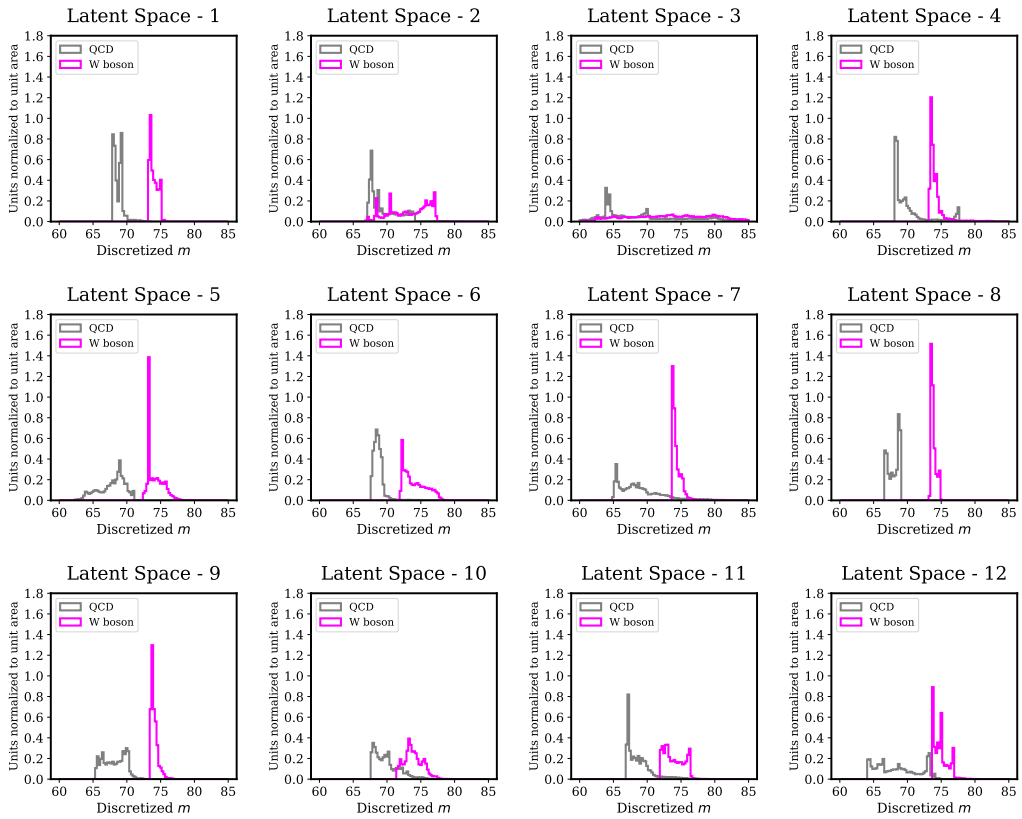


Figure 22: Mass distributions for each latent space value.

We visualize the curves in Figures 22 and 23 by plotting the average W boson image and the average QCD image for each latent space value and the difference between both images in Figure 24. We can see how there is little variation between the center images throughout different latent space values but the features of the jet images change. This illustrates that the latent space of the VAE produces W boson and QCD jet images with unique features but the difference between them are consistent throughout all latent space values.

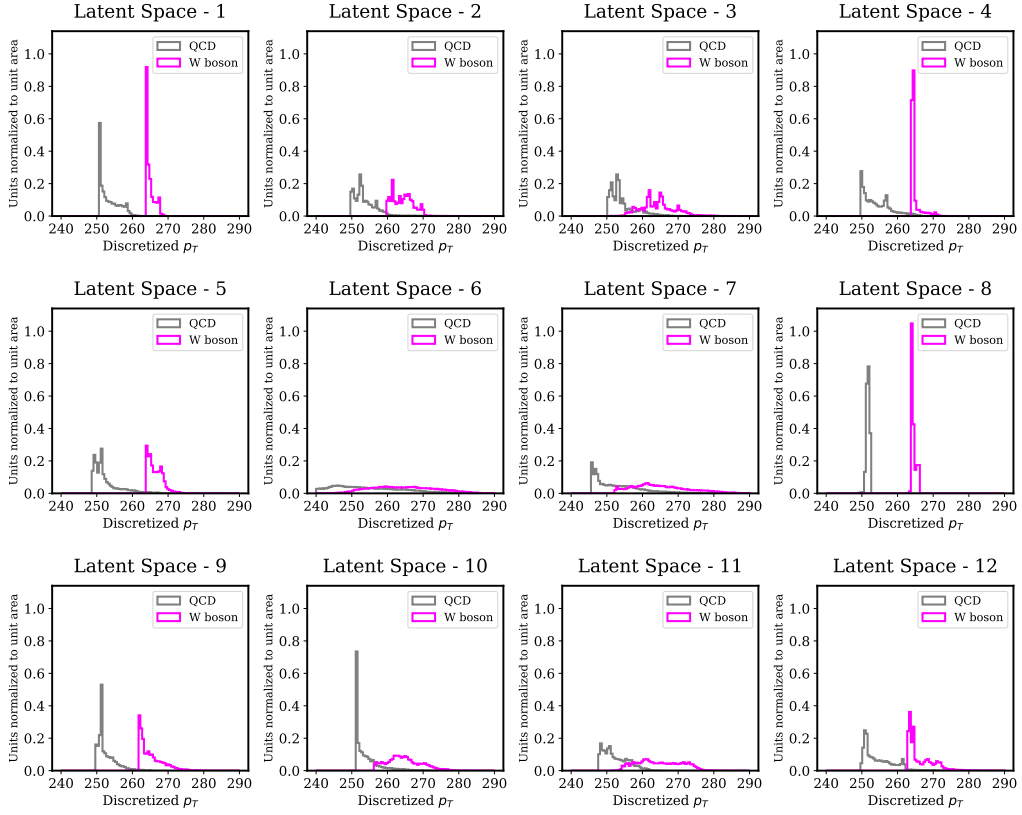


Figure 23: p_T distributions for each latent space value.

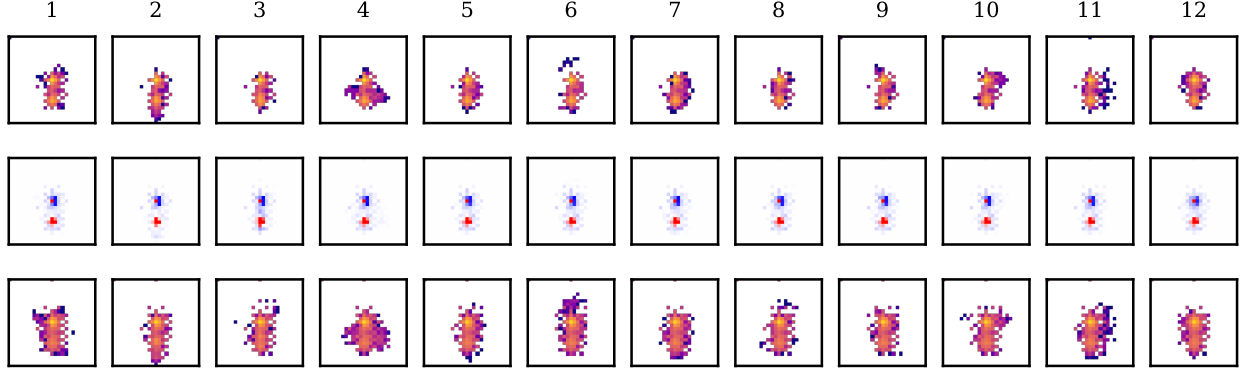


Figure 24: Average jet images for each latent space value. The top column represents the average W boson jet image, the bottom represents the average QCD jet image, and the center column is the difference between the two images. We can observe how the W boson and QCD jet images have unique properties but the difference between them remain relatively the same throughout all latent space values.

5 Speed Comparison

Speed is a very important factor when developing a deep generative model for high energy physics. Due to the increasing reliance on simulation at the LHC, generative models need to be not only accurate in simulating detail data, but they also have to be fast. The current most popular generative model to generate jet images is the GAN. To test the speed of the VAE, we compare the total time it takes to generate 300,000 jet images and its rate of producing jet images with the LAGAN in Table 4 and Figure 25.

Table 4: Speed Comparison of LAGAN and VAE

	Events/s	Time for 300k Events (s)
LAGAN (CPU)	714	420
LAGAN (GPU)	4102	73
VAE (CPU)	2176	138
VAE (GPU)	24209	12

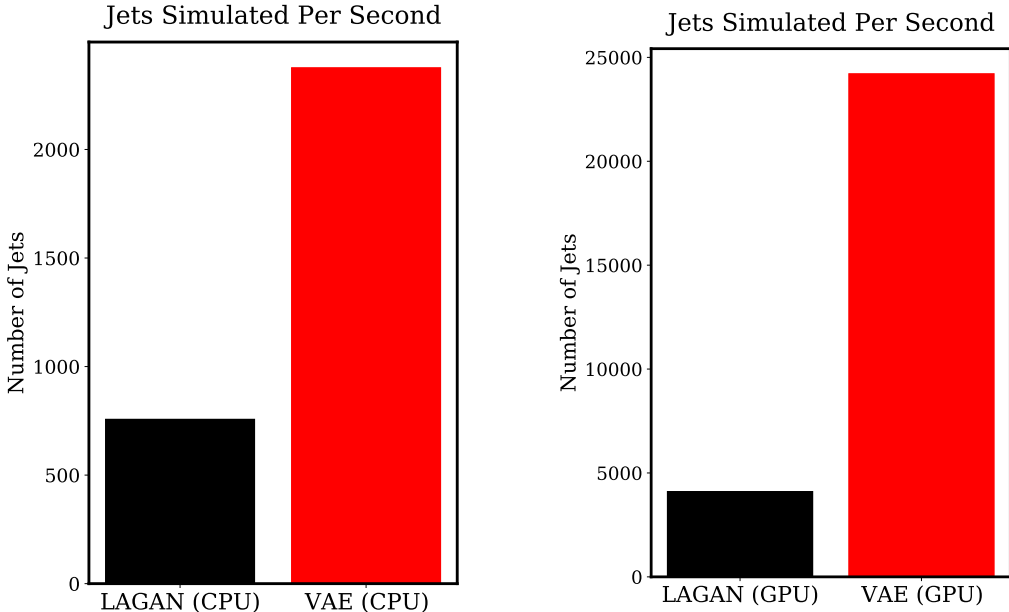


Figure 25: Speed Comparison between LAGAN and VAE using both a CPU and a GPU.

The VAE model, using a GPU, is shown to be around 6 times faster than the LAGAN. This is most likely the case because the LAGAN depends on locally-connected layers to generate the radiation patterns and jet prongs of its jet images. Locally-connected layers are computationally expensive, therefore, it would make sense that the LAGAN will take up

more time to generate its jet images. This contrasts our model, which uses convolutional layers to obtain the distinct features of jet images.

In addition to the simulation speed of VAEs, the VAE is also shown to be easy to train. Because the structure of the VAE does not require adversarial training, which is known to be difficult to train, it can optimize relatively more smoothly. This ultimately encourages the exploration of hybrids of GANs and VAEs.

6 Conclusion

In this paper, we have successfully implemented a variational autoencoder to simulate realistic jet images. The model we propose is able to reproduce key characteristics of Pythia jet images. Some of these characteristics include mass, p_T , N-subjettiness, and pixel intensity. In addition to showing the accuracy of the VAE, we explored the latent space and saw how it can be used to produce unique distributions. This can be potentially used for other tasks such as jet tagging, where we can assess how certain taggers perform when given a wide variety of jet images produced by the VAE. The VAE we propose is also demonstrated to be faster than the LAGAN due to its lack of reliance on computationally expensive architectures such as locally-connected layers.

This paper also demonstrated the effectiveness of the feature perceptual loss for computer-vision-related techniques in high energy physics. This can be applied to not only other types of generative models, but they can also be applied to other algorithms for specific tasks such as autoencoders for anomaly detection. The feature perceptual can replace any standard distance metric loss such as the mean squared error, making it a powerful, yet simple technique for high energy physics tasks that require image recognition.

GANs have been known to produce images that are sharper than VAEs. We explore new and well-established VAE techniques in machine learning literature to ultimately create a fast algorithm that is comparable to the GAN in performance. Because the GAN and VAE have their own unique advantages, exploring hybrid models seem to be a promising direction for future research. To summarize, the VAE we propose is ultimately a fast, easy-to-train, and accurate generative model that can be used to generate realistic high energy physics data.

Acknowledgments

I would like to thank my mentor Dr. David Shih for guiding this research. He has provided useful discussions, background material on machine learning in high energy physics, feedback on the manuscript, and overall great support. I would also like to thank Dr. Benjamin Nachman for his valuable feedback on the manuscript and for insightful discussion.

References

- [1] Luke de Oliveira, Michela Paganini, and Benjamin Nachman. Learning particle physics by example: location-aware generative adversarial networks for physics synthesis, 2017. arXiv: [1701.05927 \[stat.ML\]](https://arxiv.org/abs/1701.05927).
- [2] Riccardo Di Sipio, Michele Faucci Giannelli, Sana Katabchi Haghishat, and Serena Palazzo. Dijetgan: a generative-adversarial network approach for the simulation of qcd dijet events at the lhc, 2019. arXiv: [1903.02433 \[hep-ex\]](https://arxiv.org/abs/1903.02433).
- [3] SHiP Collaboration. Fast simulation of muons produced at the ship experiment using generative adversarial networks, 2019. arXiv: [1909.04451 \[physics.ins-det\]](https://arxiv.org/abs/1909.04451).
- [4] Michela Paganini, Luke de Oliveira, and Benjamin Nachman. Calogan: simulating 3d high energy particle showers in multi-layer electromagnetic calorimeters with generative adversarial networks, 2017. arXiv: [1712.10321 \[hep-ex\]](https://arxiv.org/abs/1712.10321).
- [5] Sydney Otten, Sascha Caron, Wieske de Swart, Melissa van Beekveld, Luc Hendriks, Caspar van Leeuwen, Damian Podareanu, Roberto Ruiz de Austri, and Rob Verheyen. Event generation and statistical sampling for physics with deep generative models and a density information buffer, 2019. arXiv: [1901.00875 \[hep-ph\]](https://arxiv.org/abs/1901.00875).
- [6] Stefano Carrazza and Frédéric A. Dreyer. Lund jet images from generative and cycle-consistent adversarial networks, 2019. arXiv: [1909.01359 \[hep-ph\]](https://arxiv.org/abs/1909.01359).
- [7] Michela Paganini, Luke de Oliveira, and Benjamin Nachman. Accelerating science with generative adversarial networks: an application to 3d particle showers in multi-layer calorimeters, 2017. arXiv: [1705.02355 \[hep-ex\]](https://arxiv.org/abs/1705.02355).
- [8] Saúl Alonso-Monsalve and Leigh H. Whitehead. Image-based model parameter optimization using model-assisted generative adversarial networks, 2018. arXiv: [1812.00879 \[cs.CV\]](https://arxiv.org/abs/1812.00879).

- [9] Jesus Arjona Martinez, Thong Q Nguyen, Maurizio Pierini, Maria Spiropulu, and Jean-Roch Vlimant. Particle generative adversarial networks for full-event simulation at the lhc and their application to pileup description, 2019. arXiv: [1912.02748 \[hep-ex\]](https://arxiv.org/abs/1912.02748).
- [10] Marco Bellagente, Anja Butter, Gregor Kasieczka, Tilman Plehn, and Ramon Winterhalder. How to gan away detector effects, 2019. arXiv: [1912.00477 \[hep-ph\]](https://arxiv.org/abs/1912.00477).
- [11] Anja Butter, Tilman Plehn, and Ramon Winterhalder. How to gan lhc events, 2019. arXiv: [1907.03764 \[hep-ph\]](https://arxiv.org/abs/1907.03764).
- [12] Bobak Hashemi, Nick Amin, Kaustuv Datta, Dominick Olivito, and Maurizio Pierini. Lhc analysis-specific datasets with generative adversarial networks, 2019. arXiv: [1901.05282 \[hep-ex\]](https://arxiv.org/abs/1901.05282).
- [13] Viktoria Chekalina, Elena Orlova, Fedor Ratnikov, Dmitry Ulyanov, Andrey Ustyuzhanin, and Egor Zakharov. Generative models for fast calorimeter simulation.lhcb case, 2018. arXiv: [1812.01319 \[physics.data-an\]](https://arxiv.org/abs/1812.01319).
- [14] F Carminati, A Gheata, G Khattak, P Mendez Lorenzo, S Sharan, and S Vallecorsa. Three dimensional generative adversarial networks for fast simulation. *Journal of Physics: Conference Series*, 1085:032016, September 2018. DOI: [10.1088/1742-6596/1085/3/032016](https://doi.org/10.1088/1742-6596/1085/3/032016). URL: <https://doi.org/10.1088%2F1742-6596%2F1085%2F3%2F032016>.
- [15] Pasquale Musella and Francesco Pandolfi. Fast and accurate simulation of particle detectors using generative adversarial networks, 2018. arXiv: [1805.00850 \[hep-ex\]](https://arxiv.org/abs/1805.00850).
- [16] Dawit Belayneh, Federico Carminati, Amir Farbin, Benjamin Hooberman, Gulruk Khattak, Miaoyuan Liu, Junze Liu, Dominick Olivito, Vitória Barin Pacela, Maurizio Pierini, Alexander Schwing, Maria Spiropulu, Sofia Vallecorsa, Jean-Roch Vlimant, Wei Wei, and Matt Zhang. Calorimetry with deep learning: particle simulation and reconstruction for collider physics, 2019. arXiv: [1912.06794 \[physics.ins-det\]](https://arxiv.org/abs/1912.06794).
- [17] Luke de Oliveira, Michela Paganini, and Benjamin Nachman. Controlling physical attributes in gan-accelerated simulation of electromagnetic calorimeters, 2017. arXiv: [1711.08813 \[hep-ex\]](https://arxiv.org/abs/1711.08813).
- [18] Jan M. Pawłowski and Julian M. Urban. Reducing autocorrelation times in lattice simulations with generative adversarial networks, 2018. arXiv: [1811.03533 \[hep-lat\]](https://arxiv.org/abs/1811.03533).
- [19] Harold Erbin and Sven Krippendorf. Gans for generating eft models, 2018. arXiv: [1809.02612 \[cs.LG\]](https://arxiv.org/abs/1809.02612).

[20] Martin Erdmann, Jonas Glombitza, and Thorben Quast. Precise simulation of electromagnetic calorimeter showers using a wasserstein generative adversarial network, 2018. arXiv: [1807.01954 \[physics.ins-det\]](https://arxiv.org/abs/1807.01954).

[21] Y. Alanazi, P. Ambrozewicz, M. P. Kuchera, Y. Li, T. Liu, R. E. McClellan, W. Melnitchouk, E. Pritchard, M. Robertson, N. Sato, R. Strauss, and L. Velasco. Ai-based monte carlo event generator for electron-proton scattering, 2020. arXiv: [2008.03151 \[hep-ph\]](https://arxiv.org/abs/2008.03151).

[22] Denis Derkach, Nikita Kazeev, Fedor Ratnikov, Andrey Ustyuzhanin, and Alexandra Volokhova. Cherenkov detectors fast simulation using neural networks, 2019. arXiv: [1903.11788 \[hep-ex\]](https://arxiv.org/abs/1903.11788).

[23] Deja, Kamil, Trzcin’ski, Tomasz, and Graczykowski, Lukasz. Generative models for fast cluster simulations in the tpc for the alice experiment. *EPJ Web Conf.*, 214:06003, 2019. DOI: [10.1051/epjconf/201921406003](https://doi.org/10.1051/epjconf/201921406003). URL: <https://doi.org/10.1051/epjconf/201921406003>.

[24] Kai Zhou, Gergely Endrődi, Long-Gang Pang, and Horst Stöcker. Regressive and generative neural networks for scalar field theory, 2018. arXiv: [1810.12879 \[hep-lat\]](https://arxiv.org/abs/1810.12879).

[25] S. Vallecorsa. Generative models for fast simulation. *Journal of Physics: Conference Series*, 1085:022005, September 2018. DOI: [10.1088/1742-6596/1085/2/022005](https://doi.org/10.1088/1742-6596/1085/2/022005). URL: <https://doi.org/10.1088%2F1742-6596%2F1085%2F2%2F022005>.

[26] Martin Erdmann, Lukas Geiger, Jonas Glombitza, and David Schmidt. Generating and refining particle detector simulations using the wasserstein distance in adversarial networks, 2018. arXiv: [1802.03325 \[astro-ph.IM\]](https://arxiv.org/abs/1802.03325).

[27] Anja Butter, Sascha Diefenbacher, Gregor Kasieczka, Benjamin Nachman, and Tilman Plehn. Ganplifying event samples, 2020. arXiv: [2008.06545 \[hep-ph\]](https://arxiv.org/abs/2008.06545).

[28] Josh Cogan, Michael Kagan, Emanuel Strauss, and Ariel Schwartzman. Jet-images: computer vision inspired techniques for jet tagging, 2014. arXiv: [1407.5675 \[hep-ph\]](https://arxiv.org/abs/1407.5675).

[29] Patrick T. Komiske, Eric M. Metodiev, and Matthew D. Schwartz. Deep learning in color: towards automated quark/gluon jet discrimination, 2016. arXiv: [1612.01551 \[hep-ph\]](https://arxiv.org/abs/1612.01551).

[30] Luke de Oliveira, Michael Kagan, Lester Mackey, Benjamin Nachman, and Ariel Schwartzman. Jet-images – deep learning edition, 2015. arXiv: [1511.05190 \[hep-ph\]](https://arxiv.org/abs/1511.05190).

[31] Diederik P Kingma and Max Welling. Auto-encoding variational bayes, 2013. arXiv: [1312.6114 \[stat.ML\]](https://arxiv.org/abs/1312.6114).

[32] Christian Ledig, Lucas Theis, Ferenc Huszar, Jose Caballero, Andrew Cunningham, Alejandro Acosta, Andrew Aitken, Alykhan Tejani, Johannes Totz, Zehan Wang, and Wenzhe Shi. Photo-realistic single image super-resolution using a generative adversarial network, 2016. arXiv: [1609.04802 \[cs.CV\]](https://arxiv.org/abs/1609.04802).

[33] Ting-Chun Wang, Ming-Yu Liu, Jun-Yan Zhu, Andrew Tao, Jan Kautz, and Bryan Catanzaro. High-resolution image synthesis and semantic manipulation with conditional gans, 2017. arXiv: [1711.11585 \[cs.CV\]](https://arxiv.org/abs/1711.11585).

[34] Ali Razavi, Aaron van den Oord, and Oriol Vinyals. Generating diverse high-fidelity images with vq-vae-2, 2019. arXiv: [1906.00446 \[cs.LG\]](https://arxiv.org/abs/1906.00446).

[35] Arash Vahdat and Jan Kautz. Nvae: a deep hierarchical variational autoencoder, 2020. arXiv: [2007.03898 \[stat.ML\]](https://arxiv.org/abs/2007.03898).

[36] Kai Yi, Yi Guo, Yanan Fan, Jan Hamann, and Yu Guang Wang. Cosmavae: variational autoencoder for cmb image inpainting, 2020. arXiv: [2001.11651 \[eess.IV\]](https://arxiv.org/abs/2001.11651).

[37] Yunchen Pu, Zhe Gan, Ricardo Henao, Xin Yuan, Chunyuan Li, Andrew Stevens, and Lawrence Carin. Variational autoencoder for deep learning of images, labels and captions, 2016. arXiv: [1609.08976 \[stat.ML\]](https://arxiv.org/abs/1609.08976).

[38] Ishaan Gulrajani, Kundan Kumar, Faruk Ahmed, Adrien Ali Taiga, Francesco Visin, David Vazquez, and Aaron Courville. Pixelvae: a latent variable model for natural images, 2016. arXiv: [1611.05013 \[cs.LG\]](https://arxiv.org/abs/1611.05013).

[39] Taoli Cheng, Jean-François Arguin, Julien Leissner-Martin, Jacinthe Pilette, and Tobias Golling. Variational autoencoders for anomalous jet tagging, 2020. arXiv: [2007.01850 \[hep-ph\]](https://arxiv.org/abs/2007.01850).

[40] I. Higgins, Loïc Matthey, A. Pal, C. Burgess, Xavier Glorot, M. Botvinick, S. Mohamed, and Alexander Lerchner. Beta-vae: learning basic visual concepts with a constrained variational framework. In *ICLR*, 2017.

[41] Aishik Ghosh. Deep generative models for fast shower simulation in ATLAS. Technical report ATL-SOFT-PROC-2019-007, CERN, Geneva, June 2019. doi: [10.1088/1742-6596/1525/1/012077](https://doi.org/10.1088/1742-6596/1525/1/012077). URL: <https://cds.cern.ch/record/2680531>.

- [42] Erik Buhmann, Sascha Diefenbacher, Engin Eren, Frank Gaede, Gregor Kasieczka, Anatolii Korol, and Katja Krüger. Getting high: high fidelity simulation of high granularity calorimeters with high speed, 2020. arXiv: [2005.05334 \[physics.ins-det\]](https://arxiv.org/abs/2005.05334).
- [43] Huaibo Huang, Zhihang Li, Ran He, Zhenan Sun, and Tieniu Tan. Introvae: introspective variational autoencoders for photographic image synthesis, 2018. arXiv: [1807.06358 \[cs.LG\]](https://arxiv.org/abs/1807.06358).
- [44] Aaron van den Oord, Oriol Vinyals, and Koray Kavukcuoglu. Neural discrete representation learning, 2017. arXiv: [1711.00937 \[cs.LG\]](https://arxiv.org/abs/1711.00937).
- [45] Jaechang Lim, Seongok Ryu, Jin Woo Kim, and Woo Youn Kim. Molecular generative model based on conditional variational autoencoder for de novo molecular design. *Journal of cheminformatics*, 10(1):1–9, 2018.
- [46] Stanislau Semeniuta, Aliaksei Severyn, and Erhardt Barth. A hybrid convolutional variational autoencoder for text generation, 2017. arXiv: [1702.02390 \[cs.CL\]](https://arxiv.org/abs/1702.02390).
- [47] Sam Sinai, Eric Kelsic, George M. Church, and Martin A. Nowak. Variational auto-encoding of protein sequences, 2017. arXiv: [1712.03346 \[q-bio.QM\]](https://arxiv.org/abs/1712.03346).
- [48] Amir Khoshaman, Walter Vinci, Brandon Denis, Evgeny Andriyash, Hossein Sadeghi, and Mohammad H. Amin. Quantum variational autoencoder, 2018. arXiv: [1802.05779 \[quant-ph\]](https://arxiv.org/abs/1802.05779).
- [49] Slava Voloshynovskiy, Mouad Kondah, Shideh Rezaifar, Olga Taran, Taras Holotyak, and Danilo Jimenez Rezende. Information bottleneck through variational glasses, 2019. arXiv: [1912.00830 \[cs.CV\]](https://arxiv.org/abs/1912.00830).
- [50] Riddhish Bhalodia, Iain Lee, and Shireen Elhabian. Dpvaes: fixing sample generation for regularized vaes, 2019. arXiv: [1911.10506 \[cs.LG\]](https://arxiv.org/abs/1911.10506).
- [51] Lester Mackey, Benjamin Nachman, Ariel Schwartzman, and Conrad Stansbury. Fuzzy jets, 2015. arXiv: [1509.02216 \[hep-ph\]](https://arxiv.org/abs/1509.02216).
- [52] Patrick T. Komiske, Eric M. Metodiev, and Jesse Thaler. The metric space of collider events, 2019. arXiv: [1902.02346 \[hep-ph\]](https://arxiv.org/abs/1902.02346).
- [53] Barry M. Dillon, Darius A. Faroughy, Jernej F. Kamenik, and Manuel Szewc. Learning the latent structure of collider events, 2020. arXiv: [2005.12319 \[hep-ph\]](https://arxiv.org/abs/2005.12319).
- [54] Barry M. Dillon, Darius A. Faroughy, and Jernej F. Kamenik. Uncovering latent jet substructure, 2019. arXiv: [1904.04200 \[hep-ph\]](https://arxiv.org/abs/1904.04200).

[55] Lucio Mwinmaarong Dery, Benjamin Nachman, Francesco Rubbo, and Ariel Schwartzman. Weakly supervised classification in high energy physics, 2017. arXiv: [1702.00414 \[hep-ph\]](https://arxiv.org/abs/1702.00414).

[56] Eric M. Metodiev, Benjamin Nachman, and Jesse Thaler. Classification without labels: learning from mixed samples in high energy physics, 2017. arXiv: [1708.02949 \[hep-ph\]](https://arxiv.org/abs/1708.02949).

[57] Patrick T. Komiske, Eric M. Metodiev, Benjamin Nachman, and Matthew D. Schwartz. Learning to classify from impure samples with high-dimensional data, 2018. arXiv: [1801.10158 \[hep-ph\]](https://arxiv.org/abs/1801.10158).

[58] Jack H. Collins, Kiel Howe, and Benjamin Nachman. Anomaly detection for resonant new physics with machine learning, 2018. arXiv: [1805.02664 \[hep-ph\]](https://arxiv.org/abs/1805.02664).

[59] Jack H Collins, Kiel Howe, and Benjamin Nachman. Extending the bump hunt with machine learning, 2019. arXiv: [1902.02634 \[hep-ph\]](https://arxiv.org/abs/1902.02634).

[60] Maxim Borisyak and Nikita Kazeev. Machine learning on data with splot background subtraction, 2019. arXiv: [1905.11719 \[cs.LG\]](https://arxiv.org/abs/1905.11719).

[61] Timothy Cohen, Marat Freytsis, and Bryan Ostdiek. (machine) learning to do more with less, 2017. arXiv: [1706.09451 \[hep-ph\]](https://arxiv.org/abs/1706.09451).

[62] Patrick T. Komiske, Eric M. Metodiev, and Jesse Thaler. An operational definition of quark and gluon jets, 2018. arXiv: [1809.01140 \[hep-ph\]](https://arxiv.org/abs/1809.01140).

[63] Eric M. Metodiev and Jesse Thaler. On the topic of jets: disentangling quarks and gluons at colliders, 2018. arXiv: [1802.00008 \[hep-ph\]](https://arxiv.org/abs/1802.00008).

[64] Oz Amram and Cristina Mantilla Suarez. Tag n' train: a technique to train improved classifiers on unlabeled data, 2020. arXiv: [2002.12376 \[hep-ph\]](https://arxiv.org/abs/2002.12376).

[65] Olmo Cerri, Thong Q. Nguyen, Maurizio Pierini, Maria Spiropulu, and Jean-Roch Vlimant. Variational autoencoders for new physics mining at the large hadron collider, 2018. arXiv: [1811.10276 \[hep-ex\]](https://arxiv.org/abs/1811.10276).

[66] Marco Farina, Yuichiro Nakai, and David Shih. Searching for new physics with deep autoencoders, 2018. arXiv: [1808.08992 \[hep-ph\]](https://arxiv.org/abs/1808.08992).

[67] Theo Heimel, Gregor Kasieczka, Tilman Plehn, and Jennifer M Thompson. Qcd or what?, 2018. arXiv: [1808.08979 \[hep-ph\]](https://arxiv.org/abs/1808.08979).

[68] Benjamin Nachman, Luke de Oliveira, and Michela Paganini. Pythia Generated Jet Images for Location Aware Generative Adversarial Network Training, February 2017. DOI: [10.17632/4r4v785rgx.1](https://doi.org/10.17632/4r4v785rgx.1). URL: <https://doi.org/10.17632/4r4v785rgx.1>.

[69] Torbjörn Sjöstrand, Stephen Mrenna, and Peter Skands. A brief introduction to pythia 8.1, 2007. arXiv: [0710.3820 \[hep-ph\]](https://arxiv.org/abs/0710.3820).

[70] Torbjorn Sjostrand, Stephen Mrenna, and Peter Skands. Pythia 6.4 physics and manual, 2006. arXiv: [hep-ph/0603175 \[hep-ph\]](https://arxiv.org/abs/hep-ph/0603175).

[71] Matteo Cacciari, Gavin P. Salam, and Gregory Soyez. Fastjet user manual, 2011. arXiv: [1111.6097 \[hep-ph\]](https://arxiv.org/abs/1111.6097).

[72] Kihyuk Sohn, Honglak Lee, and Xinchen Yan. Learning structured output representation using deep conditional generative models. In *NIPS*, pages 3483–3491, 2015. URL: <http://papers.nips.cc/paper/5775-learning-structured-output-representation-using-deep-conditional-generative-models>.

[73] Xianxu Hou, Linlin Shen, Ke Sun, and Guoping Qiu. Deep feature consistent variational autoencoder, 2016. arXiv: [1610.00291 \[cs.CV\]](https://arxiv.org/abs/1610.00291).

[74] Justin Johnson, Alexandre Alahi, and Li Fei-Fei. Perceptual losses for real-time style transfer and super-resolution, 2016. arXiv: [1603.08155 \[cs.CV\]](https://arxiv.org/abs/1603.08155).

[75] François Chollet et al. Keras. <https://keras.io>, 2015.

[76] Martín Abadi, Ashish Agarwal, Paul Barham, Eugene Brevdo, Zhifeng Chen, Craig Citro, Greg S. Corrado, Andy Davis, Jeffrey Dean, Matthieu Devin, Sanjay Ghemawat, Ian Goodfellow, Andrew Harp, Geoffrey Irving, Michael Isard, Yangqing Jia, Rafal Jozefowicz, Lukasz Kaiser, Manjunath Kudlur, Josh Levenberg, Dandelion Mané, Rajat Monga, Sherry Moore, Derek Murray, Chris Olah, Mike Schuster, Jonathon Shlens, Benoit Steiner, Ilya Sutskever, Kunal Talwar, Paul Tucker, Vincent Vanhoucke, Vijay Vasudevan, Fernanda Viégas, Oriol Vinyals, Pete Warden, Martin Wattenberg, Martin Wicke, Yuan Yu, and Xiaoqiang Zheng. TensorFlow: large-scale machine learning on heterogeneous systems, 2015. URL: <https://www.tensorflow.org/>. Software available from tensorflow.org.

[77] Luke de Oliveira, Michela Paganini, and Benjamin Nachman. Pre-trained Model Weights for Location Aware Generative Adversarial Networks [arxiv/1701.05927], March 2017. DOI: [10.5281/zenodo.400706](https://doi.org/10.5281/zenodo.400706). URL: <https://doi.org/10.5281/zenodo.400706>.

[78] Jesse Thaler and Ken Van Tilburg. Identifying boosted objects with n-subjettiness, 2010. arXiv: [1011.2268 \[hep-ph\]](https://arxiv.org/abs/1011.2268).